

# Noncontact laser vibrometry-based fence-like arrays with wavefield filtering-assisted adaptive imaging algorithms for detecting multiple pits in a compact cluster

Structural Health Monitoring  
2021, Vol. 20(5) 2813–2827

© The Author(s) 2020

Article reuse guidelines:

sagepub.com/journals-permissions

DOI: 10.1177/1475921720976926

journals.sagepub.com/home/shm



Zhenhua Tian<sup>1</sup>, Zhaoyun Ma<sup>2</sup>, Wenfeng Xiao<sup>2</sup> and Lingyu Yu<sup>2</sup> 

## Abstract

Pitting corrosion presents challenges for ultrasonic nondestructive evaluation due to the small pit dimension. Few Lamb wave-based techniques have achieved the identification of individual pits as subwavelength wave scatterers that are densely packed in a small cluster. In this article, noncontact laser vibrometry-based fence-like arrays with wavefield filtering-assisted adaptive imaging algorithms are developed for detecting and identifying small pits in a cluster. Signals of back scattering waves induced by a cluster of subwavelength scatterers are acquired by noncontact laser Doppler vibrometry at sensing points and form a fence-like array surrounding the area of inspection. The signals are then processed by our array imaging algorithms to construct inspection images which take advantage of three techniques, including the wave mode and wave direction filters to extract single-mode back scattering Lamb waves induced by subwavelength scatterers, the pseudo-reversal propagation of back scattering waves to address the dispersion effect and improve the radial imaging resolution, and the adaptive weighting to improve the angular imaging resolution. Moreover, this work introduces the wave diffraction-related Rayleigh and Abbe limits that are conventionally used for characterizing optic lenses, for characterizing the resolution limit of Lamb wave-based arrays, and optimizing the array configuration. To validate our array imaging approach, a proof-of-concept experiment has been performed to detect a cluster of  $3 \times 3$  pits with the pit diameter of 2 mm and the interval of 2 mm in a 3.2-mm thick aluminum plate; the experimental imaging result shows that our method can identify most pits except the one at the center of the pit cluster. We believe this study will benefit the design, characterization, and optimization of Lamb wave-based arrays for subwavelength resolution imaging and enable potential applications for the noncontact inspection of hidden pitting corrosion in civil, petrochemical, nuclear, and aerospace structures.

## Keywords

Lamb waves, fence array imaging, subwavelength wave scatterers, pitting corrosion, noncontact sensing

## Introduction

Pitting corrosion is a common type of localized corrosion in engineering structures.<sup>1,2</sup> For this type of corrosion attack, small volumes of materials are removed by the chemical or electrochemical reaction to form pits, which may have saucer-like, conical, hemispherical, or other shapes.<sup>3</sup> Although only a small amount of material is corroded, the growth of pitting corrosion may lead to through-thickness pinhole damage (complete perforation of a structure) and catastrophic situations; for example, the leakage of hazardous chemicals and

<sup>1</sup>Department of Aerospace Engineering, Mississippi State University, Mississippi State, MS, USA

<sup>2</sup>Department of Mechanical Engineering, University of South Carolina, Columbia, SC, USA

### Corresponding author:

Zhenhua Tian, Department of Aerospace Engineering, Mississippi State University, Mississippi State, MS 39759, USA.

Email: tian@ae.msstate.edu

Lingyu Yu, Department of Mechanical Engineering, University of South Carolina, Columbia, SC 29208, USA.

Email: yu3@cec.sc.edu

gases from pressure vessels in energy or petrochemical industries.<sup>4,5</sup> The pitting corrosion is also known to initiate fatigue cracks in high-strength aluminum alloys, which continues to be a serious concern in the aging aircraft.<sup>6,7</sup> Compared to the uniform corrosion, the pitting corrosion is more difficult to be detected and quantitatively evaluated because pits have much smaller sizes and may present in the form of a cluster.<sup>1</sup> To detect large-size corrosion damage, imaging methods based on wavefield and wavenumber analyses have been developed.<sup>8–11</sup> The local wavenumber information of waves in the damage region allows for characterizing both the corrosion size and depth. However, as found in our recent study,<sup>11</sup> the wavenumber-based method is still difficult to resolve individual pits that are compactly distributed in a cluster. The local wavenumber information-based methods mainly use the wavenumbers of the waves from the region containing the damage and are demonstrated to detect large-size corrosion damage.

Guided waves are known for propagating long distances with low energy loss and high sensitivity to small defects in plate-like structures, rods, and pipes.<sup>12–14</sup> These features allow guided wave-based structural health monitoring (SHM) and nondestructive evaluation (NDE) methods to inspect large structures efficiently and detect small defects, such as pitting corrosion. Fromme et al.<sup>15</sup> demonstrated the application of Lamb wave-based phased arrays to detect pitting corrosion simulated by machined blind holes in a steel plate. Chen et al.<sup>16</sup> presented a sparse array using  $A_0$  Lamb waves to identify localized corrosion simulated by a small through-hole in a submerged aluminum plate. Rathod and Mahapatra<sup>17</sup> demonstrated the detection of pitting corrosion in an aluminum plate using Lamb waves generated and acquired by a circular array of piezoelectric (PZT) transducers. Besides using Lamb wave-based inspection methods for plates, guided waves have also been adopted to detect pitting corrosion in other types of structures, such as pipes and rods. Shivaraj et al.<sup>5</sup> showed that circumferential guided waves could be used for the detection of single pits simulated by drilled blind holes in pipes. Satyarnarayan et al.<sup>18</sup> demonstrated the detection of pitting corrosion in a pipe using circumferential higher-order guided waves. Zhang et al.<sup>19</sup> used the traveling time of scattering waves to localize pitting corrosion in rods. The previous guided wave-based methods listed above for detecting pitting corrosion are mostly based on the analysis of scattering guided waves induced by the pitting corrosion. Even though they can identify the location of pitting corrosion, few are able to generate high-resolution images to identify individual pits that are distributed in a compact cluster.

Lamb wave-based arrays, such as phased arrays,<sup>20–26</sup> sparse arrays,<sup>27,28</sup> and tomography arrays<sup>29–39</sup> among others,<sup>40–46</sup> use multiple sensors to acquire signals of scattering, reflection, or transmission waves. By analyzing the wave–damage interaction information in acquired signals, inspection intensity images can be constructed to identify the location and to quantify the damage. Previously, multiple Lamb wave-based arrays were developed for the detection of pitting corrosion.<sup>15–17</sup> However, those arrays were limited to finding the location of the entire pit cluster; and they did not resolve individual pits distributed in a compact cluster. In fact, Lamb wave-based methods have been challenged by multiple subwavelength scatterers that are packed in a cluster with subwavelength spatial intervals. Moreover, the performance of Lamb wave-based arrays could suffer from the multimodal and dispersive natures of Lamb waves. Although various configurations of Lamb wave-based arrays and different imaging algorithms have been developed,<sup>20–34</sup> few techniques consider the isolation of individual modes, mitigation of wave dispersion, and enabling high-resolution adaptive imaging all together. In addition, the following two aspects have not been considered in previous Lamb wave-related studies to our best knowledge. First, few studies consider the characterization of Lamb wave-based arrays from the perspective of diffraction limits and the diffraction limit-based array optimization with the goal of improving the resolution limit (i.e. the minimum resolvable distance between multiple defects). Second, although noncontact Lamb wave-based SHM and NDE methods using sensors, such as laser Doppler vibrometers and air-coupled transducers, recently attract great interests,<sup>47–54</sup> few of them consider noncontact sensing in the frequency range above 1 MHz.

This article presents noncontact laser vibrometry-based fence-like arrays with wavefield filtering-assisted adaptive imaging algorithms for detecting multiple small pits compactly distributed in a cluster. In our array design, four PZT actuators are arranged at lower, upper, right, and left sides of the damage area (i.e. the area with a pit cluster) to generate incident Lamb waves from different directions. Using a scanning laser Doppler vibrometer, signals of back scattering waves induced by the pits are acquired at multiple points to form the fence-like array. The array imaging algorithms take advantage of three techniques: (1) the wavefield filtering for extracting single-mode back scattering waves from complex waves that contain multiple wave modes and waves propagating in different directions; (2) the pseudo-reversal wave propagation based on the frequency–wavenumber dispersion relation for addressing the dispersion effect of Lamb waves and

improving the imaging resolution in the radial direction (i.e. radial imaging resolution); and (3) the adaptive weighting for improving the imaging resolution in the angular direction (i.e. angular imaging resolution). To characterize the array imaging algorithms, the wave diffraction-related Rayleigh and Abbe limits are introduced, which are conventionally used for characterizing the resolutions of optic lenses. The Rayleigh and Abbe limits are also adopted for optimizing Lamb wave-based arrays with the objective of reducing the resolution limit. A proof-of-concept experiment has been performed to validate the imaging approach and visualize pitting corrosion simulated by a cluster of  $3 \times 3$  pits (with the interval of 2 mm and the pit diameter of 2 mm) in a 3.2-mm thick aluminum plate. The remainder of this article is organized as follows: section “Wavefield filtering-assisted adaptive array imaging” presents the wavefield filtering-assisted adaptive array imaging algorithms, the diffraction limit of Lamb wave-based arrays, and the optimization of array configurations; section “Laser vibrometry-based fence-like arrays” presents the laser vibrometry-based fence-like arrays with the related sensing and imaging procedures for constructing damage inspection images; section “Experiment of detecting a compact cluster of multiple pits” presents an experimental study of detecting individual pits in a compact cluster; and section “Conclusion and discussions” concludes the article with findings, discussions, and future work.

## Wavefield filtering-assisted adaptive array imaging

This section presents the development and characterization of a wavefield filtering-assisted adaptive array imaging approach, which offers the capability for constructing high-resolution damage inspection images to distinguish multiple subwavelength scatterers that are placed close to each other. Three techniques are adopted, including the wavefield filtering, the pseudo-reversal wave propagation, and the adaptive weighting. In addition, the array imaging is characterized using data obtained through finite element simulations. The array’s resolution limit (i.e. the minimum resolvable distance between two subwavelength scatterers) is characterized by introducing the Rayleigh and Abbe limits that are typically used for the characterization of optic lenses.<sup>55</sup>

### Algorithms of the wavefield filtering-assisted adaptive array imaging

The algorithms are developed based on the configuration in Figure 1(a), which is composed of one actuator

for generating incident Lamb waves and an array of sensors for acquiring weak scattering Lamb waves induced by subwavelength scatterers (defects) in an isotropic plate. More details of the experimental setup and array implementation can be found in the sections “Laser vibrometry-based fence-like arrays and Experiment of detecting a compact cluster of multiple pits.” For the configuration in Figure 1(a), the actuator can be selected from any types of transmitters (such as round-shaped PZT wafers), which can generate circular-wavefront Lamb waves. The actuator’s position is denoted as  $\mathbf{p}_t$  in the  $x$ - $y$  Cartesian coordinate system. However, to receive Lamb waves, our configuration requires a sensing approach (such as a scanning laser Doppler vibrometer), which is able to acquire a time-space wavefield  $v(t, \mathbf{x})$  with the space resolution smaller than a half of the minimum wavelength and the time resolution smaller than a half of the minimum time period to be used. From the region where the time-space wavefield is acquired, multiple points at locations of  $[\mathbf{p}_m]_M$  ( $m = 1, 2, \dots, M$ ) are selected to serve as the sensor array; for example, a linear array shown in Figure 1(a). In addition to this simple linear array, other array configurations can be designed as well.

Figure 1(b) shows a flow chart of the array signal processing steps that fall in two categories, the wavefield filtering and the adaptive array imaging. Starting from the acquired time-space wavefield  $v(t, \mathbf{x})$  that usually contains complex waves, including waves of multiple modes, incident waves, and damage scattering waves, the Fourier transform is applied to derive a frequency-space wavefield  $V(f, \mathbf{x})$ . By further applying wavefield filtering,<sup>56–58</sup> a filtered frequency-space wavefield can be obtained, which contains only the single-mode back scattering waves; for example, a wavefield  $V_{b\_A0}(f, \mathbf{x})$  only containing  $A_0$  mode back scattering waves. The filtering process is briefly explained here for the completeness of knowledge. First, the original frequency-space wavefield  $V(f, \mathbf{x})$  is transformed to a frequency-wavenumber representation  $S(f, \mathbf{k})$  through two-dimensional (2D) Fourier transform.  $S(f, \mathbf{k})$  is then multiplied with a frequency-wavenumber window  $W(f, \mathbf{k})$  to isolate the frequency-wavenumber information  $S_{b\_A0}(f, \mathbf{k})$ , which contains the desired frequency band, magnitudes of wavenumber vectors  $|\mathbf{k}|$  and angles of wavenumber vectors  $\arg(\mathbf{k})$  for retaining the back scattering  $A_0$  waves. After the isolation, inverse 2D Fourier transform is performed to transform  $S_{b\_A0}(f, \mathbf{k})$  back to a frequency-space wavefield  $V_{b\_A0}(f, \mathbf{x})$ . The detailed procedures for wavefield filtering can be found in our previous studies.<sup>56–58</sup>

For the 2D Fourier transform used for getting a frequency-wavenumber representation  $S(f, \mathbf{k})$ , the wavenumber resolution is related to the spatial

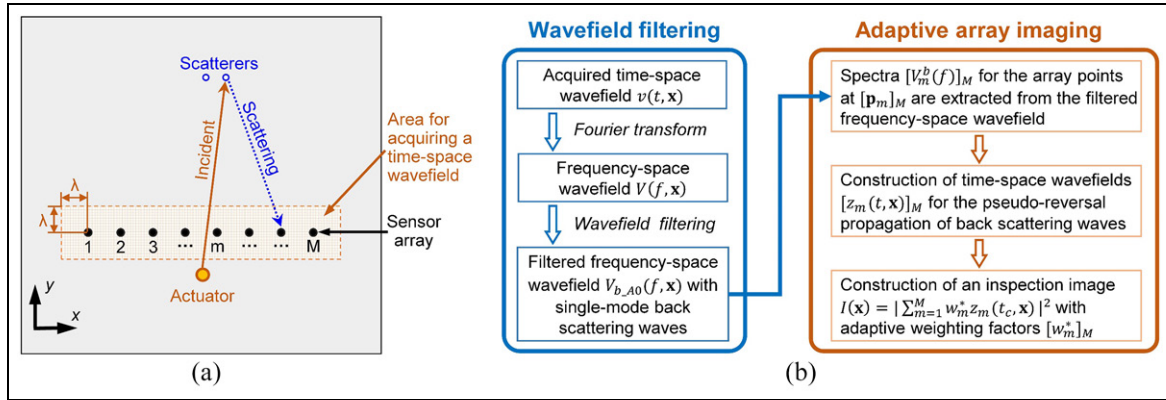


**Figure 1.** Schematics for illustrating the wavefield filtering-assisted adaptive array imaging approach. (a) A schematic of a sensing configuration composed of one actuator (brown circle) and an array of sensors (black circles) for detecting two small scatterers (blue circles) in an isotropic plate. The brown grid represents the area for acquiring a time–space wavefield that contains both incident and back scattering waves.  $M$  points located at coordinates  $[\mathbf{p}_m]_M$  are selected from the wavefield to construct a sensor array. The linear sensor array shown in the schematic is for illustration purpose; sensors distributed in other configurations can also be used. (b) A flow chart of the array signal processing steps that fall in two categories, the wavefield filtering and the adaptive array imaging.

dimension of the input wavefield. If the space dimension is larger (i.e. the area size for wavefield acquisition), the wavenumber resolution after transformation will be higher. Accordingly, the isolation of wavenumbers for single-mode backscattering waves will be easier to perform with higher accuracy. Based on our previous experiences in frequency–wavenumber analysis,<sup>56–58</sup> we suggest that the distances (from any element of the sensor array to the boundary of the region of wavefield acquisition) are set to be at least a wavelength, as illustrated in Figure 1(a). With this sensing configuration, the wavenumber resolution is high enough for extracting good quality signals containing single-mode backscattering waves. However, if the area for wavefield acquisition is too small, the wavefield filtering method may have poor wavenumber resolutions and further affect the quality of extracted signals and the final array imaging result.

The frequency–space wavefield  $V_{b,A0}(f, \mathbf{x})$  obtained through wavefield filtering is used as the input for the adaptive array imaging process. The frequency spectra  $[V_m^b(f)]_M$  at predefined sensing positions  $(\mathbf{p}_m)_M$  are extracted using the equation  $V_m^b(f) = V_{b,A0}(f, \mathbf{p}_m)$ . The extracted frequency spectra only contain the information of single-mode back scattering waves induced by defects. The processing of  $[V_m^b(f)]_M$  for constructing an inspection image has two key steps: (1) the construction of time–space wavefields  $(z_m(t, \mathbf{x}))_M$  through pseudo-reversal propagation of extracted single-mode back scattering waves and (2) the construction of an image  $I(\mathbf{x})$  by summing up all the weighted wavefields at the time  $t_c$  (time center of the input excitation signal for the actuator).

To construct a time–space wavefield  $z_m(t, \mathbf{x})$  that corresponds to the pseudo-reversal propagation of back scattering waves received by the  $m$ th receiver, we first construct the frequency–space field  $Z_m(f, \mathbf{x})$  by applying a phase shift  $-\varphi_m(f, \mathbf{x})$  that depends on the location and the wave frequency to the extracted frequency spectrum  $V_m^b(f)$  of the single-mode back scattering waves, as

$$Z_m(f, \mathbf{x}) = V_m^b(f) e^{-j\varphi_m(f, \mathbf{x})} \quad (1)$$

with

$$\varphi_m(f, \mathbf{x}) = -k(f)(|\mathbf{x} - \mathbf{p}_l| + |\mathbf{x} - \mathbf{p}_m|) \quad (2)$$

Here  $-\varphi_m(f, \mathbf{x})$  represents the phase shift for the pseudo-reversal propagation of received scattering waves, and  $k(f)$  is the Lamb wave frequency–wavenumber dispersion relation. For Lamb waves generated by the actuator at  $\mathbf{p}_l$ , as the waves travel from the actuator to the defect and then scattered waves propagate back to the  $m$ th receiver, a phase shift  $\varphi_m(f, \mathbf{x})$  occurs. Thus, by applying  $-\varphi_m(f, \mathbf{x})$  to the scattering waves spectrum  $V_m^b(f)$  through equation (1), the pseudo-reversal propagation for the  $m$ th receiver can be performed. Since the phase term  $\varphi_m(f, \mathbf{x})$  includes the frequency-dependent wavenumber  $k(f)$ , the dispersion effect (frequency-dependent wave propagation) can be mitigated and the final imaging resolution in the radial direction can be improved, as proved in our previous work.<sup>59</sup>

Through the inverse Fourier transform, frequency–space fields  $(Z_m(f, \mathbf{x}))_M$  are transformed to time–space fields  $(z_m(t, \mathbf{x}))_M$ , which can be considered as the

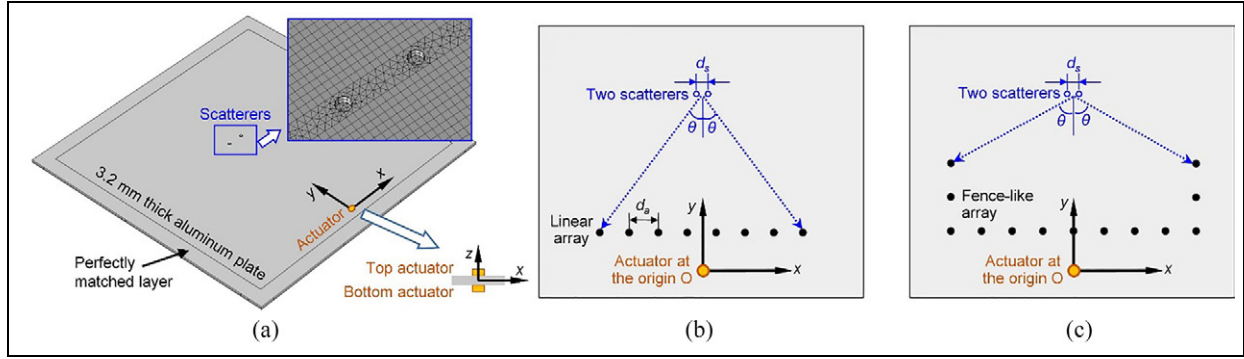


**Figure 2.** Schematics for characterizing the array imaging algorithm. (a) A schematic of the finite element model for simulating Lamb wave interaction with two subwavelength scatterers (circles in the blue box). The inset image shows the meshes in the area with two scatterers. The diameter of two scatterers is  $0.2\lambda = 3.19$  mm. The depth of scatterers is  $0.125\lambda = 2$  mm. The distance between two scatterers is denoted as  $d_s$ . As shown in the inset, two actuators attached on the top and bottom surfaces of a 3.2-mm thick aluminum plate are used to generate an incident  $A_0$  mode with a wavelength  $\lambda$  of 15.95 mm at a frequency of 100 kHz. Sensors (black circles) distributed in (b) linear and (c) fence-like array configurations are used to detect two subwavelength scatterers (blue circles) with a spacing of  $d_s$ . For simplicity, the characterization study considers arrays that are symmetric with respect to the  $y$  axis.

wavefields for the pseudo-reversal propagation of received scattering waves. At the time center  $t_c$  of the input excitation signal, the energy center of pseudo-reversal waves is supposed to be at the center of the defect, as proved in our previous work.<sup>59</sup> By summing weighted wavefields at time  $t_c$ , we can construct an image by

$$I(\mathbf{x}) = \left| \sum_{m=1}^M w_m^* z_m(t_c, \mathbf{x}) \right|^2 \quad (3)$$

where  $w_m^*$  represents the complex conjugate of the weighting factor  $w_m$ . The constructed imaging result  $I(\mathbf{x})$  is expected to show a high-intensity region to indicate the defect position. For simplicity, equation (3) can be written in the matrix format, as

$$I(\mathbf{x}) = \mathbf{w}^H(\mathbf{x}) \hat{\mathbf{R}}(\mathbf{x}) \mathbf{w}(\mathbf{x}) \quad (4)$$

where “ $H$ ” indicates the Hermitian transpose operation, and  $\hat{\mathbf{R}}(\mathbf{x})$  is a pseudo-covariance matrix defined as  $\hat{\mathbf{R}}(\mathbf{x}) = \mathbf{z}(\mathbf{x})\mathbf{z}^H(\mathbf{x})$  in which the vector  $\mathbf{z}(\mathbf{x})$  is composed of  $z_m(t_c, \mathbf{x})$ . The term  $\mathbf{w}(\mathbf{x})$  is a weighting vector composed of  $w_m$ . The weighting vector plays an important role for enhancing the imaging resolution in the angular direction. In this study, the minimum variance (MV) weighting vector is used, which is determined by

$$\mathbf{w}(\mathbf{x}) = \frac{\hat{\mathbf{R}}^{-1}(\mathbf{x})\mathbf{1}}{\mathbf{1}^T \hat{\mathbf{R}}^{-1}(\mathbf{x})\mathbf{1}} \quad (5)$$

Detailed derivations for the MV weighting vector can be found in our previous work.<sup>60</sup> Note that the mode conversion at the defect and the amplitude decay

induced by 2D energy spreading are not considered in the imaging algorithm.

### Minimum resolvable distance between two scatterers

To characterize the performance of our imaging method, we examined our method with signals obtained from a finite element model with two subwavelength scatterers in COMSOL Multiphysics. Figure 2(a) shows a schematic of the simulation model, which is a 3.2-mm thick aluminum plate with two PZT actuators (diameter 7 mm, thickness 0.2 mm) bonded on the top and bottom surfaces of the plate. By applying 100 kHz excitation signals with a phase difference of  $\pi$  to the two actuators, an incident  $A_0$  mode with a wavelength  $\lambda$  of 15.95 mm can be generated in the plate. To reduce the reflections by plate edges, a perfectly matched layer<sup>61,62</sup> surrounding the plate is used. The top surface of the plate has two small circular-shaped blind holes as weak scatterers with the same subwavelength-scale diameter of  $0.2\lambda$  (3.19 mm) and the same subwavelength-scale depth of  $0.125\lambda$  (2 mm). The distance between the centers of two scatterers is denoted as  $d_s$ . Simulations are performed for three cases with  $d_s = 0.55\lambda$  (8.77 mm) in Case 1,  $d_s = 0.61\lambda$  (9.73 mm) in Case 2, and  $d_s = \lambda$  (15.95 mm) in Case 3.

The array imaging algorithm presented in the previous subsection is used for detecting the two subwavelength scatterers. To characterize the minimum resolvable distance between two subwavelength scatterers and optimize the distribution of array points, three different array configurations are designed, including (1) a linear array with 8 elements and an observation angle  $2\theta$  of  $47.3^\circ$ , (2) a linear array with 15

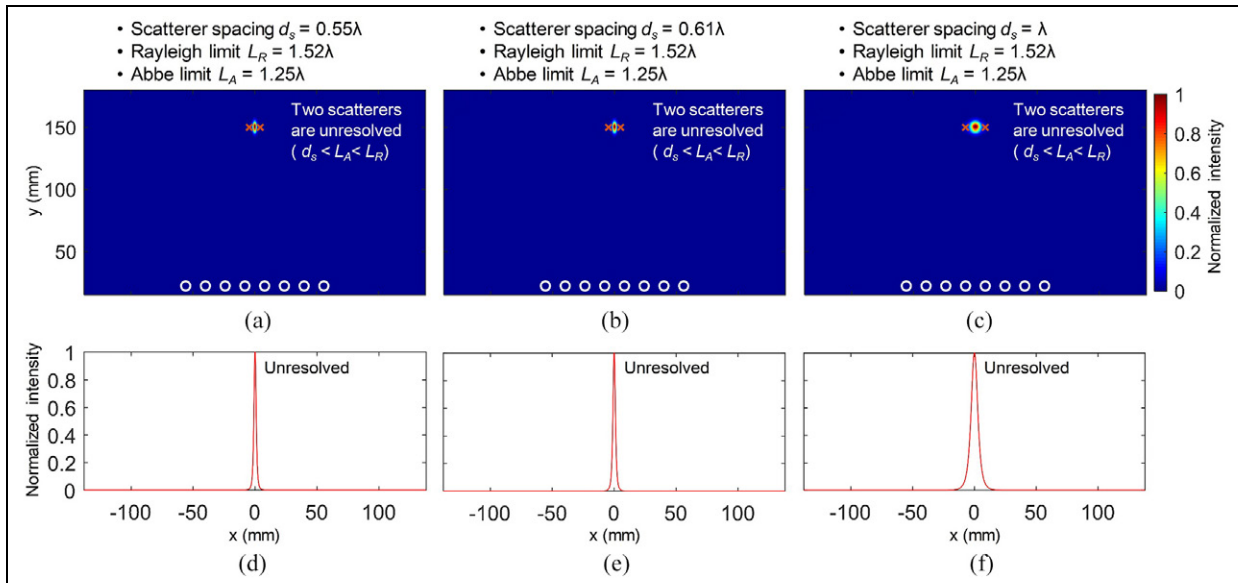


**Figure 3.** Imaging results generated by a linear array with eight elements and an observation angle  $2\theta$  of  $47.3^\circ$ . (a–c) Imaging results for the three cases with  $d_s = 0.55\lambda$ ,  $0.61\lambda$ , and  $\lambda$ , respectively. The white circles indicate locations of sensors. The “x” markers indicate actual locations of scatterers. (d–f) Distributions of image intensities with respect to x positions along the line  $y = 150$  mm for the three cases, respectively. For each case, the corresponding scatterer spacing, Rayleigh limit, and Abbe limit are listed on the top of imaging results. From the results, it can be seen that the two scatterers are unresolved in the three cases.

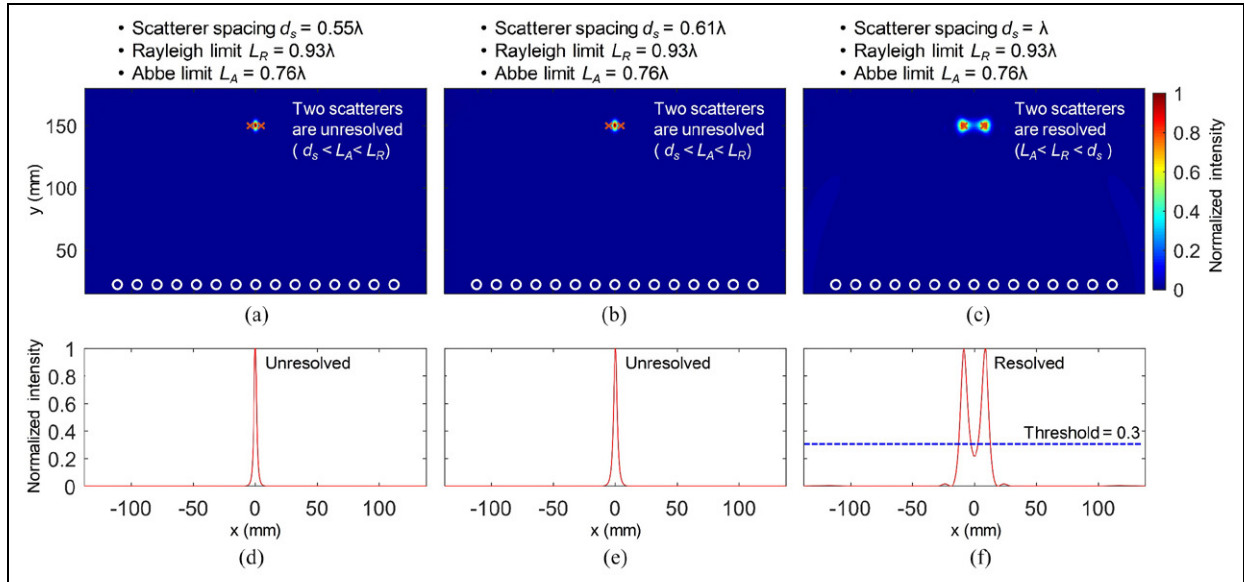
elements and an observation angle  $2\theta$  of  $82.4^\circ$ , and (3) a fence-like array with 15 elements and an observation angle  $2\theta$  of  $180^\circ$ . Note that this study limits the investigation to simple cases that arrays are symmetric with respect to a line from the actuator to the center between two scatterers. As shown in the schematics of linear and fence-like arrays (Figure 2(b) and (c)), the observation angle  $2\theta$  is defined as the maximum opening angle of the array with respect to the center between two subwavelength scatterers. This definition of observation angles for Lamb wave arrays is inspired by the way that is typically for defining the observation angle of an optic lens. In optics, the observation angle is one of the key parameters for determining the resolution of a lens, that is, the minimum resolvable distance between two light sources.<sup>55</sup> With the observation angle of  $2\theta$ , the Rayleigh and Abbe resolvable limits related to the diffraction barrier can be defined, which are  $L_R = 0.61\lambda/\sin\theta$  and  $L_A = 0.5\lambda/\sin\theta$ , respectively. These limits are usually used for characterizing the resolution of an optic lens or severing as the criteria in the design of an optic lens. In this study, we introduce the Rayleigh and Abbe limits to the Lamb wave-based arrays to characterize the minimum resolvable distance between two subwavelength scatterers and optimize the array configuration.

Figure 3(a) to (c) present the intensity images generated by a linear array with eight elements and an observation angle  $2\theta$  of  $47.3^\circ$  for the three cases with the

scatterer spacing being  $0.55\lambda$ ,  $0.61\lambda$ , and  $\lambda$ , respectively; Figure 3(d) to (f) plot the intensity distributions extracted along a line  $y = 150$  mm (passing through the centers of two scatterers) for the three cases. From the comparison among those results, we have the following findings: (1) each image shows a high-intensity spot at the center between two scatterers; (2) as the distance between two scatterers increases, the width of the high-intensity spot becomes larger; and (3) the two scatterers cannot be resolved for the three cases when the spacings between two scatterers are smaller than the Rayleigh and Abbe limits.

A linear array with 15 elements and an observation angle  $2\theta$  of  $82.4^\circ$  is also used for detecting the two scatterers. The imaging results for the three cases with the scatterer spacing being  $0.55\lambda$ ,  $0.61\lambda$ , and  $\lambda$  are given in Figure 4(a) to (c), respectively. The corresponding intensity distributions along a line  $y = 150$  mm are given in Figure 4(d) to (f). From these results, we have the following findings: (1) the two scatterers with a spacing of  $\lambda$  are resolved with a threshold of 0.3 as shown in Figure 4(f), as the spacing between scatterers is larger than the Rayleigh limit; and (2) the two scatterers with subwavelength spacings ( $0.55\lambda$  and  $0.61\lambda$ ) are still not resolved as shown in Figure 4(a) and (b), as the spacings are smaller than the Rayleigh and Abbe limits.

To further improve the imaging resolution and resolve two subwavelength scatterers with a



**Figure 4.** Imaging results generated by a linear array with 15 elements and an observation angle  $2\theta$  of  $82.4^\circ$ . (a–c) Imaging results for the three cases with  $d_s = 0.55\lambda$ ,  $0.61\lambda$ , and  $\lambda$ , respectively. The white circles indicate locations of sensors. The “x” markers indicate actual locations of scatterers. (d–f) Distributions of image intensities with respect to  $x$  positions along the line  $y = 150$  mm for the three cases, respectively. For each case, the corresponding scatterer spacing, Rayleigh limit, and Abbe limit are listed on the top of imaging results. Only in Case 3 with  $d_s = \lambda$ , the two scatterers can be resolved with a threshold of 0.3.

subwavelength spacing, the array configuration is optimized to reduce the Rayleigh limit to its minimum value. According to the equation of Rayleigh limit  $L_R = 0.61\lambda/\sin\theta$ , for a fixed wavelength  $\lambda$ , the minimum value of  $L_R$  presents at  $\sin\theta = 1$ . Hence, a fence-like array with 15 elements and an observation angle  $2\theta$  of  $180^\circ$  is designed, as illustrated by the white circles in Figure 5(a). The imaging results for the three cases with the scatterer spacing being  $0.55\lambda$ ,  $0.61\lambda$ , and  $\lambda$  are given in Figure 5(a) to (c), respectively. The corresponding intensity distributions along a line  $y = 150$  mm are given in Figure 5(d) to (f). The imaging results show that the two scatterers can be resolved in all the three cases. By comparing all the images, we have the following findings: (1) when the spacing between the two scatterers is larger than or equal to the Rayleigh limit ( $L_R \leq d_s$ ), the two scatterers can be clearly distinguished with a low threshold of 0.3; (2) when the spacing is between the Rayleigh and Abbe limits ( $L_A < d_s < L_R$ ), the two scatterers are still distinguishable with a high threshold around 0.9.

Our characterization study in the above covers three scenarios:  $d_s < L_A < L_R$ ,  $L_A < d_s < L_R$ , and  $L_A < L_R < d_s$ . These imaging results given in Figures 3 to 5 prove that the minimum resolvable distance of a Lamb wave array highly depends on the observation angle  $2\theta$ . This finding provides a guidance for designing Lamb arrays with high imaging resolutions to resolve multiple small scatterers that are close to each other.

## Laser vibrometry-based fence-like arrays

This section presents the implementation of the array imaging algorithms developed in section “Wavefield filtering-assisted adaptive array imaging” and the development of laser vibrometry-based fence-like arrays that take advantage of noncontact laser-based Lamb wave sensing. Moreover, the array arrangements presented in section “Wavefield filtering-assisted adaptive array imaging” are further improved by introducing four actuators arranged at the lower, right, upper, and left sides of the region of interest (area with defects) and a fence-like sensor array that is surrounding the region of interest, as shown in Figure 6. This array configuration allows to achieve the maximum observation angle and high imaging resolutions in both  $x$  and  $y$  dimensions. In addition to the array configuration, the sensing and imaging procedures for the laser vibrometry-based fence-like arrays are presented in detail.

### Configuration of laser vibrometry-based fence-like arrays

The array design presented in section “Wavefield filtering-assisted adaptive array imaging” has been proved to distinguish subwavelength scatterers that are horizontally arranged along the  $x$  direction. However, for practical scenarios, the positions of scatterers usually remain unknown and the scatterers could form a

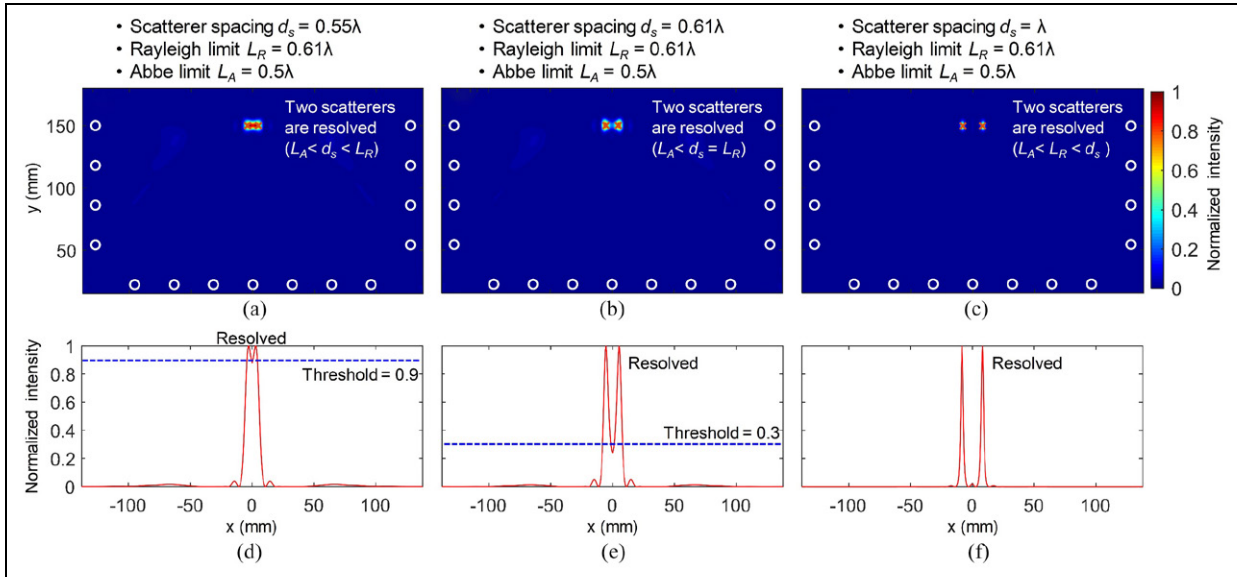


**Figure 5.** Imaging results generated by a fence-like array with 15 elements and an observation angle  $2\theta$  of  $180^\circ$ . (a–c) Imaging results for the three cases with  $d_s = 0.55\lambda$ ,  $0.61\lambda$ , and  $\lambda$ , respectively. The white circles indicate locations of sensors. The “x” markers indicate actual locations of scatterers. (d–f) Distributions of image intensities with respect to  $x$  positions along the line  $y = 150$  mm for three imaging results in (a–c). For each case, the corresponding scatterer spacing, Rayleigh limit, and Abbe limit are listed on the top of imaging results. For all three cases, the two scatterers are successfully resolved.

complex cluster. A sensing method that can address such general situations while achieving high imaging resolutions in both the  $x$  and  $y$  dimensions is desired. Therefore, an improved array configuration is designed (Figure 6) and implemented with a PZT–scanning laser Doppler vibrometry (SLDV) system that can generate incident Lamb waves and acquire complex time–space wavefields of Lamb waves in the test structure.

As shown in Figure 6, four PZT actuators  $T_{low}$ ,  $T_{right}$ ,  $T_{up}$ , and  $T_{left}$  at the lower, right, upper, and left sides of the region of interest are adopted for generating interrogation waves from four different directions. However, a noncontact SLDV (model: Polytec PSV-400-M2) is adopted to acquire out-of-plane displacements/velocities of Lamb waves propagating the in-test structure based on the Doppler effect by setting the laser beam normal to the test structure. More information about the noncontact laser Doppler vibrometry can be found in our previous study.<sup>50</sup> Through point-by-point measurement at multiple scanning points in a customized area (brown-gridded region in Figure 6), a time–space wavefield  $v(t, \mathbf{x})$  in that area can be acquired. During the wavefield acquisition, the spatial scanning resolution should be smaller than a half of the minimum wavelength, to capture the wavenumber information of Lamb waves to be used. The time sampling rate should be at least twice of the maximum frequency of Lamb waves to be adopted, to capture the wave frequency information. On completion of

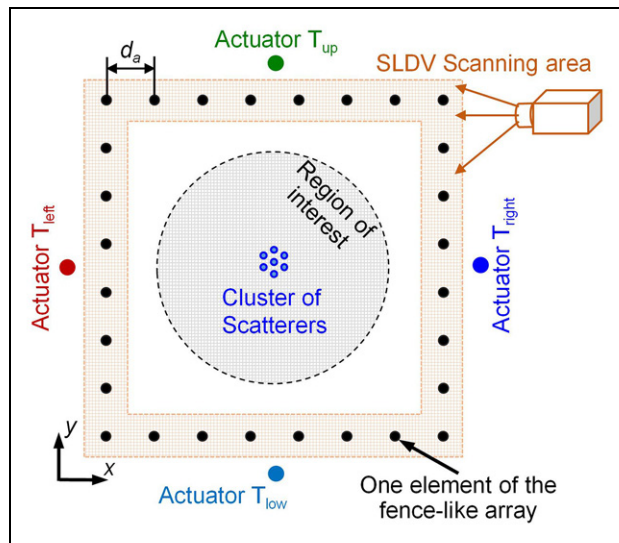


**Figure 6.** Configuration of a laser vibrometry-based fence-like array. Four actuators  $T_{low}$ ,  $T_{right}$ ,  $T_{up}$ , and  $T_{left}$  are arranged at the lower, right, upper, and left sides of the scanning area to generate incident waves. The region of interest with a cluster of scatterers is surrounded by the SLDV scanning area (brown-gridded area). The black circle inside the scanning area represents a possible selection of scanning points for constructing a fence-like array.

acquiring a time–space wavefield  $v(t, \mathbf{x})$  in the scanning area, multiple scanning points (illustrated by black circles in Figure 6) are selected from the scanning area to



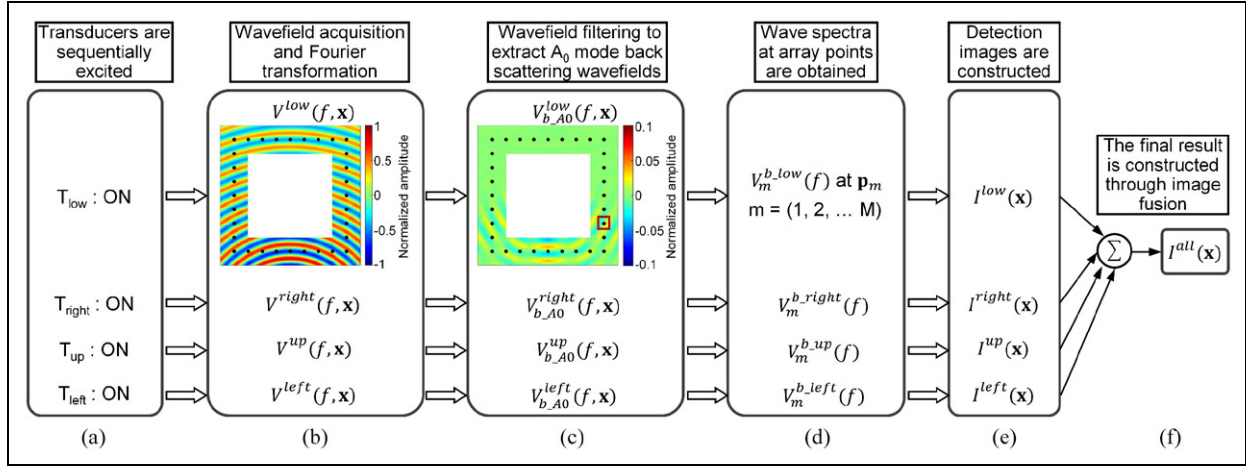


**Figure 7.** A flow chart for showing the sensing and signal processing procedures to construct a fused inspection image using a laser vibrometry-based fence-like array. (a) Four transducers are sequentially excited. (b) Time–space wavefields in the scanning area are acquired by the SLDV, and then Fourier transform is applied to obtain frequency–space wavefields. (c) Frequency–space wavefields of back scattering  $A_0$  waves are extracted by applying wavefield filtering to the wavefields in (b). (d) Frequency spectra for all the array points are extracted from the frequency–space wavefields of back scattering  $A_0$  waves. (e) Individual inspection images are constructed for the four cases with  $T_{low}$ ,  $T_{right}$ ,  $T_{up}$ , and  $T_{left}$  at ON state. (f) The final imaging result is constructed through image fusion.

form a fence-like array surrounding the region of interest (area with multiple scatterers in Figure 6). We suggest that the distances from any element of the array to the boundary of the SLDV scanning area are set to at least a wavelength.

### Sensing and imaging procedures for laser vibrometry-based fence-like arrays

To construct an inspection image with the laser vibrometry-based fence-like array, Figure 7 presents a flow chart of the sensing and signal processing procedures, which have six key steps from (a) wave generation to (f) construction of a fused inspection image. As shown in Figure 7, in the Step (a), one of the four PZT actuators is turned ON for generating incident waves. Let us use the first row with  $T_{low}$  at the ON state as an example. When the actuator  $T_{low}$  is turned ON, all the other actuators will be at the OFF state. In the Step (b), the frequency–space wavefield  $V^{low}(f, \mathbf{x})$  in the pre-defined scanning area is obtained by acquiring a time–space wavefield  $v^{low}(t, \mathbf{x})$  through noncontact laser Doppler vibrometry and then applying Fourier transform to the acquired time–space wavefield. In the Step (c), the frequency–space wavefield  $V_{b,A0}^{low}(f, \mathbf{x})$  for back scattering  $A_0$  waves induced by defects is extracted by applying wavefield filtering<sup>56</sup> on the frequency–space wavefield obtained in the Step (b). Through the Step (d), one can further extract the frequency spectra  $[V_m^{b,low}(f)]_M$  for the selected array points located at  $[\mathbf{p}_m]_M$  from the filtered frequency–space wavefield using

the relation  $V_m^{b,low}(f) = V_{b,A0}^{low}(f, \mathbf{p}_m)$ . In the Step (e), an intensity image  $I^{low}(\mathbf{x})$  can be constructed using the array imaging algorithm presented in section “Wavefield filtering-assisted adaptive array imaging” and the extracted frequency spectra  $[V_m^{b,low}(f)]_M$ . By repeating the Steps (a–e) for rest cases that the PZT actuators  $T_{right}$ ,  $T_{up}$ , and  $T_{left}$  are set to the ON state one by one, we can construct individual intensity images  $I^{right}(\mathbf{x})$ ,  $I^{up}(\mathbf{x})$ , and  $I^{left}(\mathbf{x})$ . In the last Step (f) of the flow chart, one can construct the final inspection image  $I^{all}(\mathbf{x})$  by fusing the four individual images. From the constructed final image through fusion in the Step (f), we will be able to characterize defects in the area surrounded by the fence-like array.

### Experiment of detecting a compact cluster of multiple pits

In this section, an experiment is performed to demonstrate and validate the developed noncontact laser vibrometry-based fence-like array and the wavefield filtering-assisted adaptive array imaging algorithms. The experimental study also demonstrates the capability of the array for resolving multiple small pits that are distributed in a compact cluster.

#### Experimental setup for detecting a pit cluster

A schematic and a photograph of the experimental setup are shown in Figure 8(a) and (b), respectively. The test specimen is an aluminum 6061 T6 plate

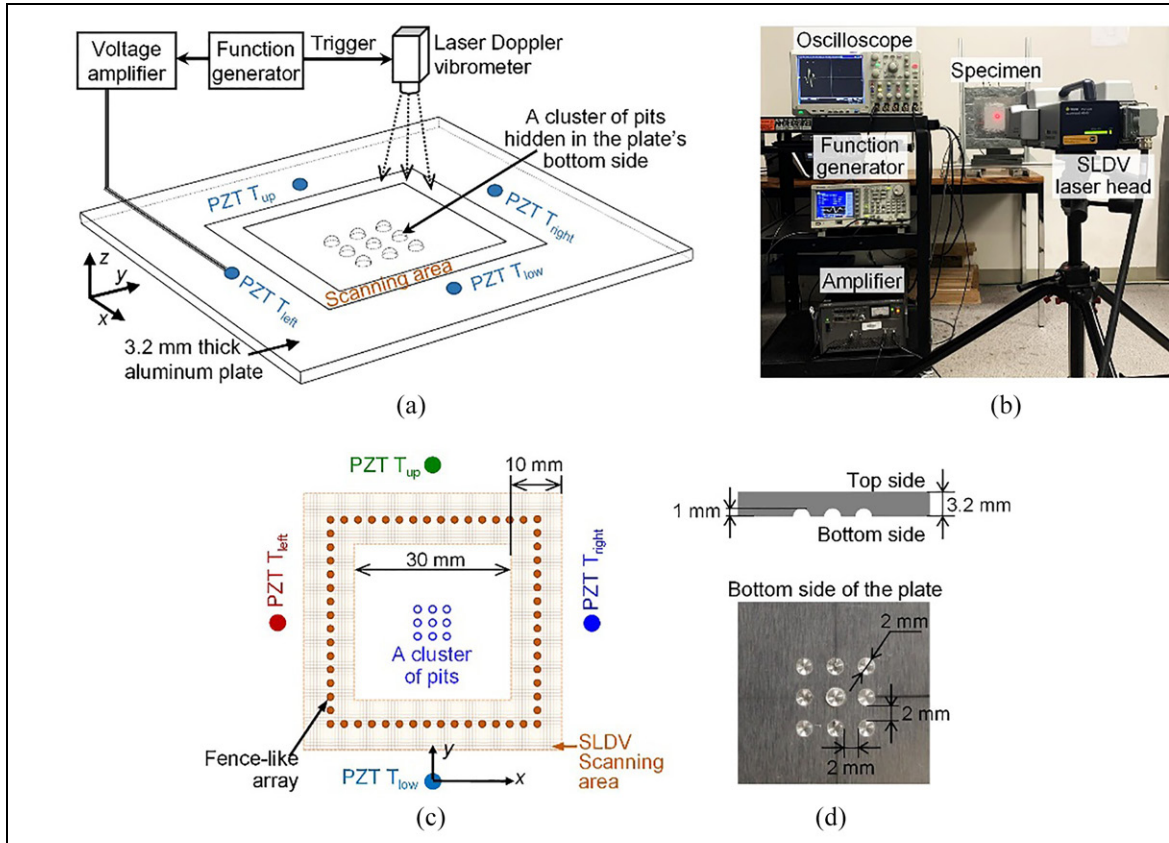


**Figure 8.** Experimental setup for detecting a pit cluster using a laser vibrometry-based fence-like array. (a) A schematic of the overall experimental setup for imaging a compact cluster of  $3 \times 3$  identical pits hidden in the bottom side of a 3.2-mm thick aluminum plate. Four PZTs  $T_{low}$ ,  $T_{right}$ ,  $T_{top}$ , and  $T_{left}$  are bonded on the top side of the plate for generating incident waves. The SLDV is used to acquire a time–space wavefield in the scanning area. (b) A photograph of the experimental setup. (c) The layout of a fence-like array (black circles) surrounding the area of interest with a cluster of small pits. (d) Top: a schematic of the plate cross-section with multiple pits; Bottom: a photograph taken from the bottom side of the plate showing  $3 \times 3$  pits. Each pit has a hemispherical shape with a diameter of 2 mm and a depth of 1 mm. In the  $x$  and  $y$  directions, the interval between adjacent pits is 2 mm.

( $610 \times 610 \times 3.2 \text{ mm}^3$ ) with a cluster of  $3 \times 3$  small pits in the bottom side of the plate to simulate pitting corrosion. Each pit has a hemispherical shape with a diameter of 2 mm; the intervals between edges of adjacent pits are 2 mm in both  $x$  and  $y$  directions, as shown in Figure 8(d). The diameter and interval are very close to the wavelength of 1.8 mm for the 1.6 MHz  $A_0$  mode that is used for this experiment. Four round PZT actuators (APC 851 by American Piezo, diameter of 7 mm, thickness of 0.2 mm) are bonded on the plate to generate incident Lamb waves at the frequency of 1.6 MHz. An arbitrary function generator (Tektronix AFG3022C) is adopted to generate the excitation signal, which is amplified to 40 Vpp by a voltage amplifier (NF HAS4014). An SLDV (model: Polytec PSV-400-M2) is used to measure the out-of-plane displacements of Lamb waves over a customized scanning area in the front surface of the plate. The space resolution of the

SLDV scanning is 0.4 mm and the time sampling rate is 12.8 MHz.

Figure 8(c) shows the sensing layout of the fence-like array surrounding the area of interest with a  $3 \times 3$  cluster of small pits. A Cartesian coordinate system with the origin  $O$  at the center of the actuator  $T_{low}$  is chosen as a reference for the sensing layout in Figure 8(c). In this Cartesian coordinate system, the coordinates for the four actuators  $T_{low}$ ,  $T_{right}$ ,  $T_{top}$ , and  $T_{left}$  are (0, 0), (60, 60), (0, 120), and (−60, 60) mm, respectively. The center of the pitting cluster is at (0, 60) mm. The sensing points of the fence-like array are distributed on the boundary of a  $40 \times 40 \text{ mm}^2$  square with the center at (0, 60) mm. The SLDV scanning area is defined as a 10 mm wide band (brown gridded region). The center of the scanning band falls on the boundary of the  $40 \times 40 \text{ mm}^2$  square. Please note that only the shaded band area is scanned for wavefield acquisition

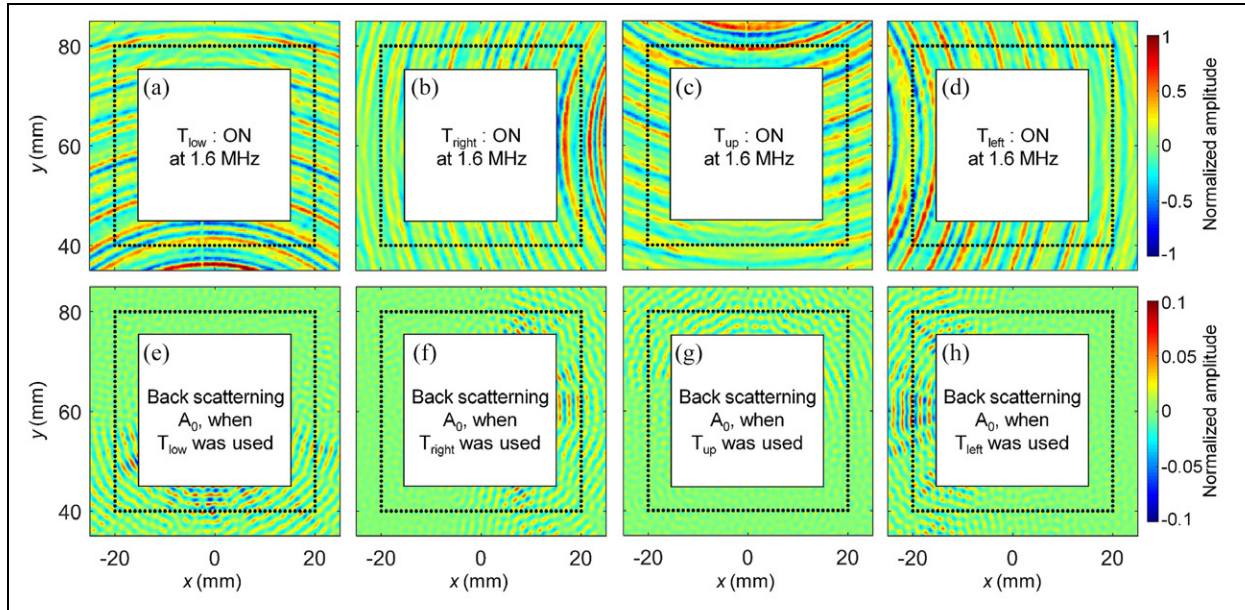


**Figure 9.** Acquired original and filtered wavefields in the scanning area at the frequency of 1.6 MHz. (a–d) Acquired wavefields by the SLDV, when  $T_{low}$ ,  $T_{right}$ ,  $T_{up}$ , and  $T_{left}$  are at the ON state, respectively. These wavefields contain both incident and back scattering waves. (e–h) Wavefields of back scattering  $A_0$  waves obtained by applying wavefield filtering to the four wavefields in (a–d), respectively. The black dots indicate locations of sensors in a fence-like array.

since our array imaging algorithm does not need to use the wavefield inside the band area (i.e. the inside white region without shading in Figure 8(c)) for the sake of reducing data acquisition time.

### Detection and imaging results

Using the laser vibrometry-based fence-like array and the Steps (a) and (b) in Figure 7, four wavefields  $V^{low}(\mathbf{x})$ ,  $V^{right}(\mathbf{x})$ ,  $V^{up}(\mathbf{x})$ , and  $V^{left}(\mathbf{x})$  at the excitation frequency 1.6 MHz are obtained, as shown in Figure 9(a) to (d). These wavefields contain both the incident and scattering Lamb waves induced by the pit cluster. By applying wavefield filtering to the obtained wavefields through the Step (c) in Figure 7, the wavefields  $V_{b-40}^{low}(\mathbf{x})$ ,  $V_{b-40}^{right}(\mathbf{x})$ ,  $V_{b-40}^{up}(\mathbf{x})$ , and  $V_{b-40}^{left}(\mathbf{x})$  of back scattering  $A_0$  waves are obtained as shown in Figure 9(e) to (h). The filtered wavefields clearly show weak back scattering waves induced by the pit cluster. From the filtered wavefields, four sets of wave spectra  $[V_m^{b-low}(f)]_M$ ,  $[V_m^{b-right}(f)]_M$ ,  $[V_m^{b-up}(f)]_M$ , and  $[V_m^{b-left}(f)]_M$  are then extracted at multiple points (black dots in Figure 9), which are distributed along the boundary of a  $40 \times 40 \text{ mm}^2$  square with an interval of 1 mm. These selected points form a fence-like array, and their corresponding extracted spectra are further processed for the construction of individual inspection images through the Step (e) in Figure 7.

Figure 10(a) to (d) present the four intensity images that are constructed with the extracted four sets of spectra  $[V_m^{b-low}(f)]_M$ ,  $[V_m^{b-right}(f)]_M$ ,  $[V_m^{b-up}(f)]_M$ , and  $[V_m^{b-left}(f)]_M$ , respectively. These four intensity images correspond to the four cases with  $T_{low}$ ,  $T_{right}$ ,  $T_{top}$ , and  $T_{left}$  at the ON state, respectively. When the actuator  $T_{low}$  is at the ON state, the imaging result in Figure 10(a) shows three high-intensity spots, whose positions agree well with the locations of three pits in the third row of the  $3 \times 3$  pit cluster (represented by red circles in the Figure 10(a)). However, the rest six pits in the first and second rows are hard to be seen from the imaging result in Figure 10(a), for the reason that incident and scattering wave pathways for those six pits are affected by the three pits in the third row. On one hand, the energy of incident waves that can arrive to the first and second rows of pits is very low, as the incident energy has been reduced by the third row of pits by wave scattering. On other hand, it is difficult for back scattering waves induced by pits in the first and second rows effectively propagating to the sensor array, due to the influence of pits in the third row. Therefore, four actuators arranged in the lower, right, upper, and left sides of the damage area are used. By fusing the corresponding array imaging results shown in Figure 10(a) to (d), the intensity image in Figure 10(e) is constructed. Compared to individual imaging results, the fused imaging result shows more

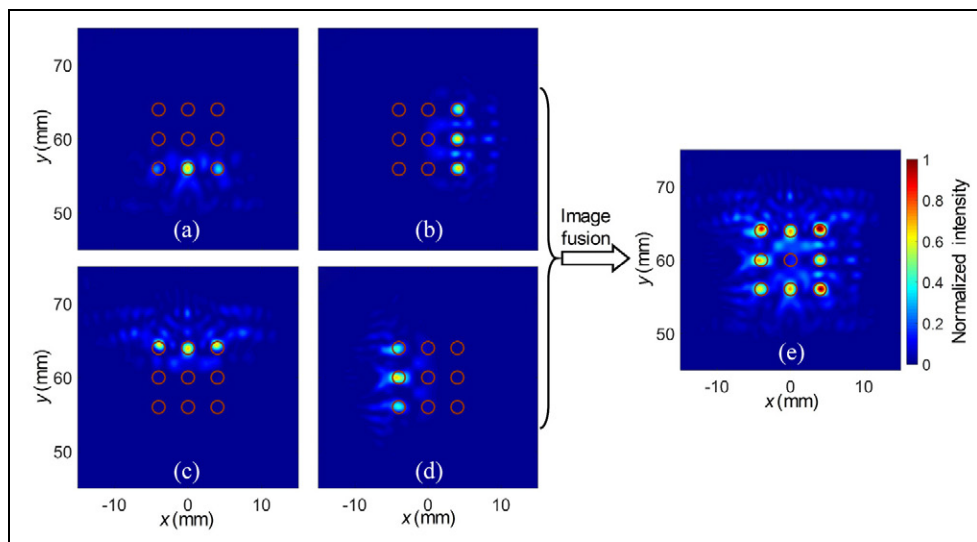


**Figure 10.** Constructed imaging results using a fence-like array. (a–d) Individual imaging results when  $T_{low}$ ,  $T_{right}$ ,  $T_{upper}$ , and  $T_{left}$  are used, respectively. (e) The final imaging result constructed through the fusion of images in (a–d). The  $3 \times 3$  brown circles represent actual locations of pits in a cluster.

pits. Most pits except the one at the center of the  $3 \times 3$  pit cluster are detected in the fused imaging result. A reason for missing the center pit is that the scattering waves induced by the center pit are further scattered by the eight pits surrounding the center pit. Although the center pit in the cluster is not detected, the imaging result of our experimental study proves the capability of our fence-like array for resolving multiple small pits that are closely distributed in a cluster.

## Conclusion and discussions

This study presents noncontact laser vibrometry-based fence-like arrays with wavefield filtering-assisted adaptive imaging algorithms for constructing high-resolution inspection images that can resolve multiple small pits that are densely packed in a cluster. In our array design, four PZT actuators arranged at the lower, upper, right, and left sides of the area containing a pit cluster are sequentially fired to generate incident Lamb waves from different directions. However, a noncontact laser Doppler vibrometer is used to acquire time–space wavefields of back scattering waves induced by multiple pits. From the laser scanning area, multiple sensing points are selected to construct a fence-like array surrounding the area containing the pit cluster. By further applying our developed wavefield filtering-assisted adaptive imaging algorithms to signals acquired by the laser vibrometry-based fence-like array, an inspection image can be constructed for the identification of individual pits in a cluster.

To validate our array imaging approach, a proof-of-concept experiment has been performed through the detection of simulated pitting corrosion, that is, a cluster of  $3 \times 3$  pits with the pit diameter of 2 mm and the interval of 2 mm. Our result (Figure 10(a)) shows that when one actuator (such as  $T_{low}$ ) is used, the three pits in the third row of the corrosion cluster can be detected. The rest six pits in the first and second rows are hard to be seen from the imaging result (Figure 10(a)), as the pathways of incident and scattering waves for those six pits are affected by the three pits in the third row. Therefore, it is necessary to use multiple actuators, such as  $T_{low}$ ,  $T_{right}$ ,  $T_{upper}$ , and  $T_{left}$  arranged in the lower, right, upper, and left sides of the damage area, to construct multiple imaging results using back scattering waves in multiple directions. Through the fusion of four imaging results corresponding to the four actuators, the final fused intensity image clearly shows most pits except the one at the center of the  $3 \times 3$  pit cluster.

Compared to previous studies of Lamb wave-based array imaging, this work has contributions in multiple aspects. First, our array imaging approach is able to detect multiple pits (or scatterers) distributed in a compact cluster; however, none of the previous Lamb wave-based arrays have successfully demonstrated this capability. Second, this study presents a new imaging method, which takes advantage of the wavefield filtering to address the multimodal issue of Lamb waves, the pseudo-reversal wave propagation to address the dispersion effect and improve the radial imaging resolution, and the adaptive weighting to improve the angular

imaging resolution. Third, this study pushes the frequency of noncontact Lamb wave-based NDE to 1.6 MHz; however, the majority of previous studies<sup>44–51</sup> are limited in the frequency range below 1 MHz.

In addition to the contributions summarized in the above, this study introduces the Rayleigh and Abbe limits that are commonly used for characterizing optic lenses,<sup>55</sup> for characterizing the resolution limit, and optimizing the configurations of Lamb wave-based arrays. Our characterization study shows that the minimum resolvable distance between two subwavelength scatterers highly depends on the observation angle  $2\theta$  of an array. When the observation angle  $2\theta$  is  $180^\circ$ , the Rayleigh limit ( $L_R = 0.61\lambda/\sin\theta$ ) has the minimum value of  $0.61\lambda$  in the subwavelength scale and, accordingly, the resolvable distance between two scatterers has the minimum value. For example, the imaging result (Figure 5) constructed with simulation data shows that two subwavelength scatterers with a subwavelength spacing can be clearly resolved when the used fence-like array has an observation angle of  $180^\circ$ . In the perspective of array configuration design, our study unveils the inherent limitation of linear arrays that the array span (length of the array) needs to be very long to achieve a large observation angle. For example, to realize the  $180^\circ$  observation angle, the span of a linear array needs to be infinite. In contrast, fence-like arrays surrounding the inspection area can easily achieve the  $180^\circ$  observation angle; therefore, these fence-like arrays are able to achieve subwavelength-scale resolvable distance. We believe the array resolution characterization presented in this article can be used as a guidance for designing high-resolution arrays that are based on Lamb waves. Overall, with multiple contributions to the Lamb wave-based array imaging, we believe this article can shed new light on the design and characterization of Lamb wave-based arrays and offer great potentials for visualization and quantitative evaluation of pitting corrosion in civil, petrochemical, nuclear, and aerospace structures.

Although our array imaging approach can resolve multiple pits in a cluster, some limitations still need to be addressed. First, the laser vibrometer used in our approach has a high cost and thus limits the wide usage of our approach. To address this limitation, in the future, we will replace the laser vibrometer with a low-cost air-coupled transducer. Second, from each wavefield of back scattering waves (Figure 9(e) to (h)), it can be seen that the back scattering waves mainly present in a half of the scanning area that is close to the actuator. This means we could likely reduce the region for wavefield acquisition and the number of array elements. In the future, we will optimize the scanning area and the array configuration to reduce the signal acquisition and post-processing time. Third, our imaging

approach is still not able to detect the center pit of the  $3 \times 3$  pit cluster, as shown in Figure 10(e). A possible reason is that the scattering waves induced by the center pit are further scattered by the rest eight pits surrounding the center one. Fourth, the experimental study uses milled hemispherical dents to simulate pitting corrosion; the quantitative evaluation of realistic pitting corrosion still needs to be investigated in the future.


### Declaration of conflicting interests

The author(s) declared no potential conflicts of interest with respect to the research, authorship, and/or publication of this article.

### Funding

The author(s) disclosed receipt of the following financial support for the research, authorship, and/or publication of this article: This study was financially supported by the University of South Carolina, Mississippi State University, and Department of Energy (Grant No. DE-NE0008894).

### ORCID iD

Lingyu Yu  <https://orcid.org/0000-0002-0514-5490>

### References

1. Koch G, Varney J, Thompson N, et al. *International measures of prevention, application, and economics of corrosion technologies study*. Houston, TX: National Association of Corrosion Engineers (NACE) International, 2016.
2. Roberge PR. *Corrosion inspection and monitoring*. Hoboken, NJ: John Wiley & Sons, 2007.
3. Roberge PR. *Corrosion engineering principles and practice*. New York: McGraw-Hill, 2008.
4. Hiwatashi Y, Endoh H and Hoshimiya T. Observation and evaluation of simulated pitting corrosion by photoacoustic imaging. *Jpn J Appl Phys* 1997; 36: 3307–3311.
5. Shivaraj K, Balasubramaniam K, Krishnamurthy CV, et al. Ultrasonic circumferential guided wave for pitting-type corrosion imaging at inaccessible pipe-support locations. *J Press Vess-T Asme* 2008; 130: 021502.
6. De S, Palit Sagar S, Dey S, et al. Quantification of pitting in two tempers of 7075 aluminium alloy by non-destructive evaluation. *Corros Sci* 2010; 52: 1818–1823.
7. van der Walde K and Hillberry BM. Characterization of pitting damage and prediction of remaining fatigue life. *Int J Fatigue* 2008; 30: 106–118.
8. Flynn EB, Chong SY, Jarmer GJ, et al. Structural imaging through local wavenumber estimation of guided waves. *NDT & E Int* 2013; 59: 1–10.
9. Truong TC and Lee J-R. Thickness reconstruction of nuclear power plant pipes with flow-accelerated corrosion damage using laser ultrasonic wavenumber imaging. *Struct Health Monit* 2017; 17: 255–265.

10. Tian Z and Yu L. Damage imaging and quantification using spectral field. In: *Proceedings of the ASME 2015 conference on smart materials, adaptive structures and intelligent systems*, Colorado Springs, CO, 21–23 September 2015. New York: ASME.
11. Tian Z, Xiao W, Ma Z, et al. Dispersion curve regression: assisted wideband local wavenumber analysis for characterizing three-dimensional (3D) profiles of hidden corrosion defects. *Mech Syst Signal Pr* 2020; 150: 107347.
12. Rose JL. *Ultrasonic waves in solid media*. Cambridge: Cambridge University Press, 1999.
13. Staszewski WJ, Boller C and Tomlinson GR. *Health monitoring of aerospace structures*. Chichester: John Wiley & Sons, 2004.
14. Giurgiutiu V. *Structural health monitoring with piezoelectric wafer active sensors*. Boston, MA: Academic Press, 2008.
15. Fromme P, Wilcox PD, Lowe MJS, et al. On the development and testing of a guided ultrasonic wave array for structural integrity monitoring. *IEEE T Ultrason Ferr* 2006; 53: 777–785.
16. Chen JG, Su ZQ and Cheng L. Identification of corrosion damage in submerged structures using fundamental anti-symmetric Lamb waves. *Smart Mater Struct* 2010; 19: 015004.
17. Rathod VT and Mahapatra DR. Ultrasonic Lamb wave based monitoring of corrosion type of damage in plate using a circular array of piezoelectric transducers. *NDT & E Int* 2011; 44: 628–636.
18. Satyarnarayan L, Chandrasekaran J, Maxfield B, et al. Circumferential higher order guided wave modes for the detection and sizing of cracks and pinholes in pipe support regions. *NDT & E Int* 2008; 41: 32–43.
19. Zhang Y, Li D and Zhou Z. Time reversal method for guided waves with multimode and multipath on corrosion defect detection in wire. *Appl Sci* 2017; 7: app7040424.
20. Kim D and Philen M. Guided wave beamsteering using MFC phased arrays for structural health monitoring: analysis and experiment. *J Intell Mater Syst Struct* 2010; 21: 1011–1024.
21. Leleux A, Micheau P and Castaings M. Long range detection of defects in composite plates using Lamb waves generated and detected by ultrasonic phased array probes. *J Nondestruct Eval* 2013; 32: 200–214.
22. Yu L and Tian Z. Guided wave phased array beamforming and imaging in composite plates. *Ultrasonics* 2016; 68: 43–53.
23. Purekar AS, Pines DJ, Sundararaman S, et al. Directional piezoelectric phased array filters for detecting damage in isotropic plates. *Smart Mater Struct* 2004; 13: 838–850.
24. Malinowski P, Wandowski T, Trendafilova I, et al. A phased array-based method for damage detection and localization in thin plates. *Struct Health Monit* 2009; 8: 5–15.
25. Velichko A and Wilcox PD. Guided wave arrays for high resolution inspection. *J Acoust Soc Am* 2008; 123: 186–196.
26. Wilcox PD, Lowe M and Cawley P. Omnidirectional guided wave inspection of large metallic plate structures using an EMAT array. *IEEE T Ultrason Ferr* 2005; 52: 653–665.
27. Hall JS and Michaels JE. Minimum variance ultrasonic imaging applied to an in situ sparse guided wave array. *IEEE T Ultrason Ferr* 2010; 57: 2311–2323.
28. Michaels JE. Detection, localization and characterization of damage in plates with an in situ array of spatially distributed ultrasonic sensors. *Smart Mater Struct* 2008; 17: 035035.
29. Prasad SM, Balasubramaniam K and Krishnamurthy CV. Structural health monitoring of composite structures using Lamb wave tomography. *Smart Mater Struct* 2004; 13: N73–N79.
30. Leonard KR and Hinders MK. Lamb wave tomography of pipe-like structures. *Ultrasonics* 2005; 43: 574–583.
31. Hay TR, Royer RL, Gao HD, et al. A comparison of embedded sensor Lamb wave ultrasonic tomography approaches for material loss detection. *Smart Mater Struct* 2006; 15: 946–951.
32. Koduru JP and Rose JL. Mode controlled guided wave tomography using annular array transducers for SHM of water loaded plate like structures. *Smart Mater Struct* 2013; 22: 125021.
33. Huthwaite P and Simonetti F. High-resolution guided wave tomography. *Wave Motion* 2013; 50: 979–993.
34. Leonard KR, Malyarenko EV and Hinders MK. Ultrasonic Lamb wave tomography. *Inverse Probl* 2002; 18: 1795–1808.
35. Rao J, Ratassepp M and Zheng F. Limited-view ultrasonic guided wave tomography using an adaptive regularization method. *J Appl Phys* 2016; 120: 194902.
36. Rao J, Ratassepp M, Lisevych D, et al. On-line corrosion monitoring of plate structures based on guided wave tomography using piezoelectric sensors. *Sensors* 2017; 17: 2882.
37. Rao J, Ratassepp M and Fan Z. Quantification of thickness loss in a liquid-loaded plate using ultrasonic guided wave tomography. *Smart Mater Struct* 2017; 26: 125017.
38. Rao J, Ratassepp M and Fan Z. Investigation of the reconstruction accuracy of guided wave tomography using full waveform inversion. *J Sound Vibr* 2017; 400: 317–328.
39. Rao J, Ratassepp M and Fan Z. Guided wave tomography based on full waveform inversion. *IEEE T Ultrason Ferr Freq Contr* 2016; 63: 737–745.
40. Senesi M, Xu B and Ruzzene M. Experimental characterization of periodic frequency-steerable arrays for structural health monitoring. *Smart Mater Struct* 2010; 19: 055026.
41. Higtuti RT, Martinez-Graullera O, Martin CJ, et al. Damage characterization using guided-wave linear arrays and image compounding techniques. *IEEE T Ultrason Ferr* 2010; 57: 1985–1995.
42. Koduru JP, Momeni S and Rose JL. Phased annular array transducers for omnidirectional guided wave mode control in isotropic plate like structures. *Smart Mater Struct* 2013; 22: 125022.
43. Engholm M and Stepinski T. Direction of arrival estimation of Lamb waves using circular arrays. *Struct Health Monit* 2011; 10: 467–480.

44. Kudela P, Radzienski M, Ostachowicz W, et al. Structural health monitoring system based on a concept of Lamb wave focusing by the piezoelectric array. *Mech Syst Signal Pr* 2018; 108: 21–32.
45. Rajagopalan J, Balasubramaniam K and Krishnamurthy CV. A single transmitter multi-receiver (STMR) PZT array for guided ultrasonic wave based structural health monitoring of large isotropic plate structures. *Smart Mater Struct* 2006; 15: 1190–1196.
46. Lee SJ, Gandhi N, Hall JS, et al. Baseline-free guided wave imaging via adaptive source removal. *Struct Health Monit* 2012; 11: 472–481.
47. Staszewski WJ, Lee BC and Traynor R. Fatigue crack detection in metallic structures with Lamb waves and 3D laser vibrometry. *Meas Sci Technol* 2007; 18: 727–739.
48. Sohn H, Dutta D, Yang JY, et al. Automated detection of delamination and disbond from wavefield images obtained using a scanning laser vibrometer. *Smart Mater Struct* 2011; 20: 045017.
49. Rogge MD and Leckey CAC. Characterization of impact damage in composite laminates using guided wavefield imaging and local wavenumber domain analysis. *Ultrasonics* 2013; 53: 1217–1226.
50. Yu L and Tian Z. Lamb wave structural health monitoring using a hybrid PZT-laser vibrometer approach. *Struct Health Monit* 2013; 12: 469–483.
51. Harb MS and Yuan FG. A rapid, fully non-contact, hybrid system for generating Lamb wave dispersion curves. *Ultrasonics* 2015; 61: 62–70.
52. Kudela P, Radzienski M and Ostachowicz W. Identification of cracks in thin-walled structures by means of wave-number filtering. *Mech Syst Signal Pr* 2015; 50–51: 456–466.
53. Ambrozinski L, Stepinski T and Uhl T. Efficient tool for designing 2D phased arrays in Lamb waves imaging of isotropic structures. *J Intell Mater Syst Struct* 2015; 26: 2283–2294.
54. Hudson TB, Hou TH, Grimsley BW, et al. Imaging of local porosity/voids using a fully non-contact air-coupled transducer and laser Doppler vibrometer system. *Struct Health Monit* 2017; 16: 164–173.
55. Hecht E. *Optics*. Harlow: Pearson Education, 2017.
56. Tian Z and Yu L. Lamb wave frequency-wavenumber analysis and decomposition. *J Intell Mater Syst Struct* 2014; 25: 1107–1123.
57. Ma Z and Yu L. Lamb wave imaging with actuator network for damage quantification in aluminum plate structures. *J Intell Mater Syst Struct*. Epub ahead of print 1 September 2020. DOI: 10.1177/1045389X20952536.
58. Tian Z and Yu L. Single mode Lamb wave phased array beamforming with hybrid PZT-SLDV sensing. In: *Proceedings of the SPIE smart structures and materials + nondestructive evaluation and health monitoring 2014*, San Diego, CA, 10 April. Bellingham, WA: International Society for Optics and Photonics.
59. Tian Z, Howden S, Ma Z, et al. Pulsed laser-scanning laser Doppler vibrometer (PL-SLDV) phased arrays for damage detection in aluminum plates. *Mech Syst Signal Pr* 2019; 121: 158–170.
60. Tian Z, Yu L, Sun X, et al. Damage localization with fiber Bragg grating Lamb wave sensing through adaptive phased array imaging. *Struct Health Monit* 2019; 18: 334–344.
61. Zampolli M, Tesei A, Jensen FB, et al. A computationally efficient finite element model with perfectly matched layers applied to scattering from axially symmetric objects. *J Acoust Soc Am* 2007; 122: 1472–1485.
62. Tian Z and Yu L. Elastic phased diffraction gratings for manipulation of ultrasonic guided waves in solids. *Phys Rev Appl* 2019; 11: 024052.